

# A Terahertz nanoscale vacuum field emission transistor with an embedded gate

Yuxiang Huang<sup>1</sup>, Binbin Hong<sup>1</sup>, Ziqi Ke<sup>1</sup>, Guanqin Guo<sup>1</sup>, Fu Gao<sup>1</sup>, Jun Liang<sup>2</sup>, Minghao Lin<sup>1</sup> and Wenlong He<sup>1</sup>

<sup>1</sup> The College of Electronic and Information Engineering, The State Key Laboratory of Radio Frequency Heterogeneous Integration, Shenzhen University, Shenzhen 518060, China.

<sup>2</sup> Institute of Microscale Optoelectronics, Shenzhen University, Shenzhen 518060, China.

\* arXiv Correspondence: 2017163003@email.szu.edu.cn

**Abstract:** Nanoscale vacuum field emission transistors (nvFET) have the potential for high-power terahertz operations. In this paper, a field emission transistor with a vacuum channel and an embedded gate working in terahertz frequency range is presented. The fabrication of the device was compatible with existing CMOS and MEMS processes, and its structure was designed to have a low gate leakage current and easy parallelisation for improved carry-load capability. Full on-chip measurements of input capacitance and I-V characteristics of the transistor were carried out, and from measured data a conductance of  $66.9 \mu\text{S}$  was calculated, and hence a cut-off frequency of  $1.69 \text{ THz}$  was calculated from the fabricated nvFET.

**Keywords:** field emission transistor; simulation; fabrication; nanoscale vacuum channel

---

## 1. Introduction

Nanoscale vacuum field emission transistors (nvFETs) represent a cutting-edge topic at the intersection of vacuum electronics and micro-nano-electronics. At the nanoscale, the electric field at the surface of the source in a nvFET could be strongly modulated by the gate, thereby the on-state current could be modulated efficiently. The majority of electrons could be absorbed by the drain through a suitably designed vacuum channel[1,2]. In recent years, this type of device has attracted considerable attention from the research community due to its potential applications in RF and terahertz, microelectromechanical systems (MEMS), and irradiation stability[3–5].

For solid-state circuit devices, there is a trade-off between power and cut-off frequency, constrained by the rate of carrier saturation drift in the channel and the dielectric breakdown field strength[6]. For nvFETs, these constraints are minimal, making them particularly suitable for high-power and high-frequency operation[7]; since the channel and electrodes of nvFETs are less affected by irradiation compared to conventional MOSFET devices, nvFETs have the potential to be used in these areas such as deep-space exploration and under harsh conditions such as high temperatures and ionizing radiation[1,8,9].

A nvFET can be structured vertically or horizontally depending on whether the movement of electrons in the channel is perpendicular or horizontal to the substrate. Vertical nvFETs were one of the earlier structures proposed, as shown in Figure 1a, since in the absence of technology to define nanometre-level width patterns, it is simpler to fabricate a vertical tip as an electron source[10–12]; in 2019, a team from NASA published in *Nature electronic* the preparation of nvFETs on silicon carbide substrates, with devices that have strong irradiation stability and temperature stability[3]. A design of the finger-gate lined-drain nvFET proposed in 2021 further reduces the gate leakage current by decreasing the area of the gate in the channel, and the cutoff frequency

**Citation:** To be added by editorial staff during production.

Academic Editor: Firstname  
Lastname

Received: date

Revised: date

Accepted: date

Published: date

obtained from the simulation was 1.63 THz[5]. In 2022, Ji Xu, et al. optimised the emission performance and effective electron efficiency of vertical nvFETs[13].

For horizontal channel nvFETs, shown in Figure 1b, due to better compatibility with conventional MOS processes, back in 2012 a research team from NASA proposed the preparation of back-gate nvFETs on the same wafer by photoresist greying, and simulated capacitance yielded cutoff frequencies up to 0.46 THz[1], and in 2014 the same team achieved co-production of nvFETs and MOSFETs[14]. In 2017, nvFET with a GAA structure was proposed[15]. Horizontal nvFETs using the substrate as the gate was realised earlier for short-channel nvFETs compared to vertical nvFETs and other configurations, with repeated improvements in field emission currents and performance: in 2021, horizontal nvFETs smaller than 10 nm were realised by defining the channel and tip on the e-beam lithography pattern via FIB[16]; in the same year, the horizontal-channel non-coplanar gate structure cut-off frequency of 3.97 THz was achieved in the Simulation results show the potential of non-coplanar gate nvFETs for terahertz applications[17]. In 2023, Jae Eun Jang's team designed and prepared horizontal nvFETs with closed microcavities as channels[9]. In the same year, Ji Xu et al. performed preparation experiments to optimise the performance of the back-gate, the side-gate, and the emitter of the nvFET[18].

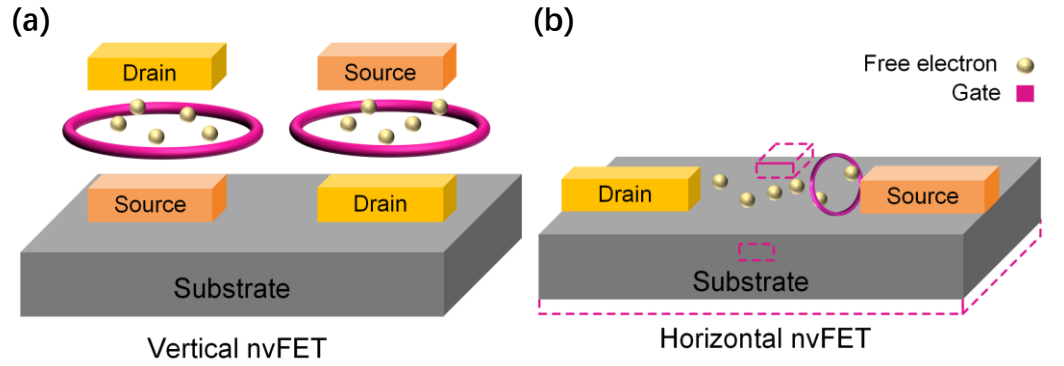


**Figure 1.** (a) Schematic of the configuration of a vertical nvFET, which can be further classified into substrate source and substrate drain; (b) Schematic of the configuration of a horizontal nvFET, which can be further classified into back-gate, buried-gate, side-gate, and ring-gate based on the gate positions

The exploration of nvFETs in RF terahertz has been widely reported, but there is a lack of research on complete on-chip testing to obtain frequency performance parameters[2]. In this paper, we propose a horizontal-channel buried-gate nvFET with terahertz-scale cutoff frequency. The buried-gate design makes it possible to obtain full-parameter on-chip measurements because this design enables a large number of devices to be connected in parallel to amplify the weak input capacitance of a single device; moreover, the gate size is smaller compared to the back-gate structure, which reduces the input capacitance and thus achieves a higher cutoff frequency; the gate is located in the dielectric buried layer and also minimizes the leakage current.

## 2. Materials and Methods

### 2.1. Simulation

The simulation software utilized in this study is COMSOL Multiphysics. This software employs an electric field physical field to solve for the device's electric field and a charged particle tracking physical field to solve for the trajectory of the field emitted electrons. The simulated devices were modelled on the same substrate as fabricating and subsequently wrapped in a vacuum infinite metric domain. This was done to obtain a model that best reflects the real physical phenomena.

The refinement of the mesh and reduction of the solution time step facilitate the acquisition of high-quality results. Mesh refinement is conducted on the cathode tip of the device, as an excessively fine mesh can significantly deplete computational memory and time, necessitating a balance between computational time and simulation quality when defining the mesh. The solution time step is configured to be adaptive, and the output time step is set to be as small as possible to enable the output of a smooth electron trajectory.

## 2.2. Fabrication

Based on the simulation results, individual sets and sets of 1,000 nvFETs were prepared, and each set of devices had probe pads adapted to the coplanar waveguide (GSG) probes. This was done to ensure that the device exteriors were grounded as much as possible, to minimize interferences in the measurements. The preparation method is a conventional semiconductor process comprising a four-pass lithography procedure, two of which are electron beam lithography. All exposure patterns are drawn by KLayout software based on the results of the simulation. The PMMA photoresist was initially spin-coated on a silicon oxide wafer, and the gate pattern was subsequently exposed using a direct-write electron beam exposure at an exposure dose of  $135 \mu\text{C}/\text{cm}^2$ , shown in Figure 2(a-b). Additionally, alignment markers were positioned at a location remote from the device in anticipation of future exposures. Following the development and fixing stages, which were conducted using the appropriate solutions, a Cr-Au layer was grown on the substrate by Electron Beam Vaporized (EBV). In this process, Cr acts as an adhesion layer for Au, while Au protects Cr from oxidation. The transistor, which had been completed with electron beam evaporation, was then placed in acetone. Subsequently, the patterned gate and the nested marker were obtained through soaking and lift-off, respectively, for use in the subsequent process, as Figure 2(c-d). Thereafter, a layer of silicon oxide was grown to serve as the gate-insulating layer, Figure 2e. A second spin coating of e-beam photoresist is employed to define the cathode pattern, which is positioned according to the previously left marker. Following the development and fixation of the image, the metal is again EBV and lift-off with acetone is utilized, Figure 2(f-h). Two UV exposures are then employed, with the UV exposures being made using a chromium mask plate fabricated on a quartz glass sheet. The purpose of the first UV exposure is to define the patterning of the gate lead electrodes, further etching of the gate insulating layer here using RIE/ICP, Figure 2(i-j); another UV exposure is used to define the patterning of the electrodes and again e-beam vaporization of the electrode material and acetone liftoff is used to obtain the final device, shown in Figure 2k. The process is shown in the flow given in Figure 2.

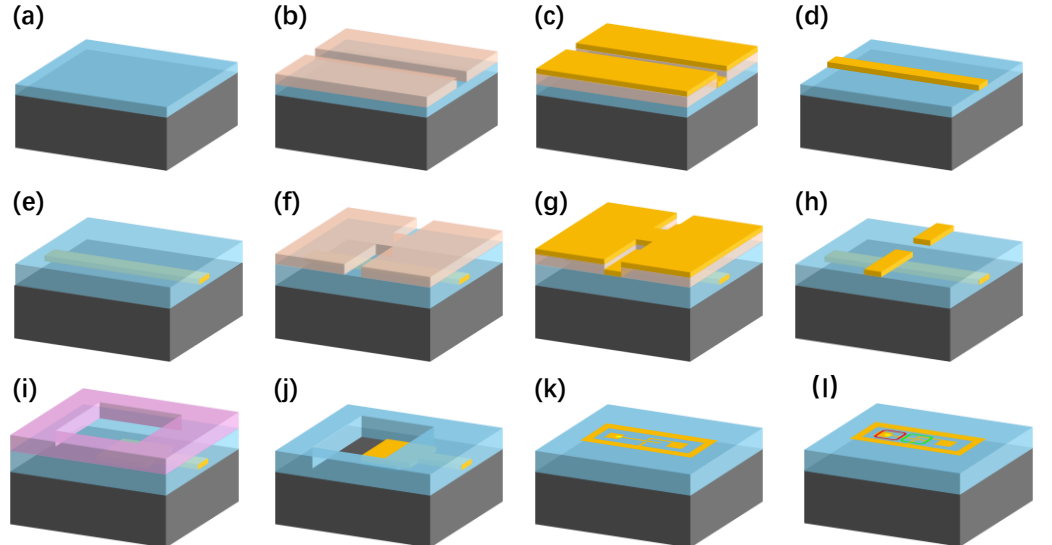


**Figure 2.** Preparation flow of the proposed nvFET, where (a) Silicon oxide wafer on intrinsic silicon is used; (b) E-beam exposure to determine the gate and marking pattern for subsequent

registration positioning, development and fixation; (c) E-beam vapour deposition of the gate metal with a thickness of less than 30 nm; (d) Peeling to remove the photoresist and the dielectric layer, which is the silicon oxide used in this study; The gate was embedded inside the dielectric layer in step (e); (f) E-beam exposure of the cathode and anode, with precise control of the cathode and gate positions according to the nesting points defined in step (b); (g-h) E-beam vapour deposition of the cathode metal, stripping. Use UV exposure to define the location of the gate entry hole in the region away from the vFET, as shown in Fig. (i); (j) Etch the gate entry hole using ICP-RIE, where the etching stops when it reaches the intrinsic silicon due to the selectivity of the etch gas and the etch rate, while the etch rate is noticeably slower in the confined region, where only a small amount of silica below the gate metal will be etched; (k) Use UV mask exposure to define the pattern of the electrodes and the large-size connecting lines, and the precipitation of thicker metals to enhance the conductivity and to allow the gate, cathode and anode to all have a reliable electrical connection to the probe; and (l) Steps (a) to (h) prepared the nanoscale structure of the transistor located at the green box line, and Steps (i) to (l) prepared the micrometre-scale structure at the red box.

### 2.3. Characterization and measurement

Once the preparation of the nvFETs was complete, it was necessary to characterize the structure of the devices using an electron microscope. This was done to ensure that the deviation of the target pattern from the prepared pattern was within acceptable limits. To characterize the structural properties of the devices, a Zeiss GeminiSEM 560 electron microscope was employed to obtain images of the device micro-nanostructures and to examine various aspects, including the quality of the electron-beam exposure, the integrity of the electrodes, and the efficacy of the surface cleaning.

Electrical testing of the devices included capacitance of the inputs to the array nvFETs and testing of individual device transmission characteristics. All electrical tests were performed on an RF vacuum probe stage with a temperature-controlled carrier stage. For capacitance measurements, the Keysight E4981A capacitance meter was used to test the input capacitance characteristics of the nvFET array, and the KEITHLEY 2636B source meter was used for the on-state and transfer characteristics tests. The test schematic is shown in Figure 3.

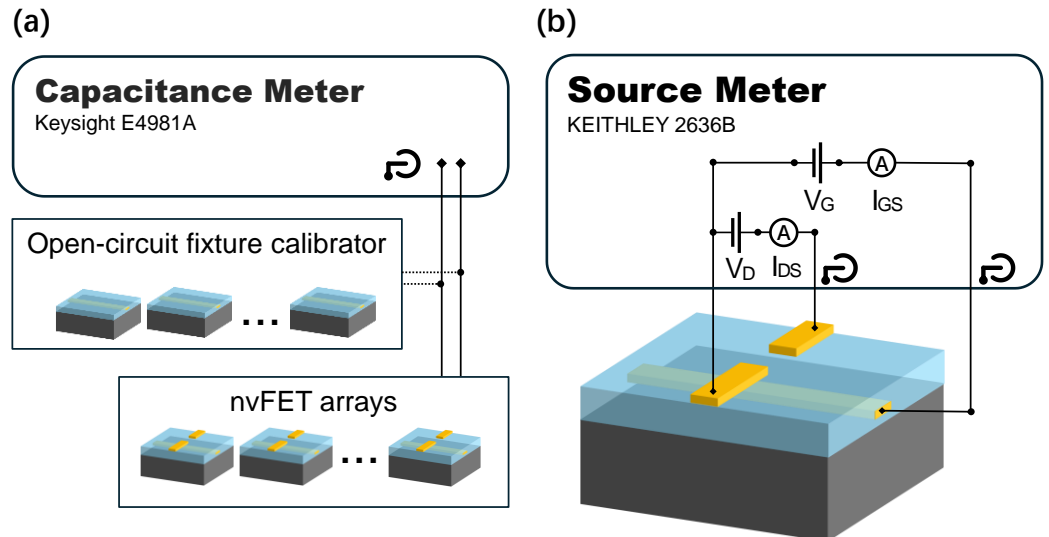


**Figure 3.** (a) Connection schematic for capacitance testing; (b) Connection schematic for the transfer and conduction characterization test.

## 3. Results

### 3.1. Simulation for optimising device geometry

According to classical theory, the free electrons in the channel during the conduction of nvFETs mainly come from the FN tunnelling effect that occurs at the surface of the source electrode[1-5,7-9]. The electrons in the conductor tunnel through a

very narrow potential barrier due to a strong electric field and reach the vacuum energy level, where they spill out of the source and become free electrons. The process of FN tunnelling is shown in the figure[19–21]. For metals, the FN tunnelling current density can be calculated according to the following Equation 1

$$J_{FN} = A_{FN} E^2 \exp(-B_{FN}/E) \quad (1a)$$

$$A_{FN} = 1.54 \times 10^{-6} / \varphi \quad (1b)$$

$$B_{FN} = 6.83 \times 10^7 \times \varphi^{1.5} \quad (1c)$$

where  $E$  is the electric field strength at the surface of the source and  $\varphi$  is the work function of the source material. To increase the on-state current  $I_{on}$  and enhance the gate control over the current  $g_m$  of the device, the usual practice for planar nvFETs is to reduce the equivalent radius of the tip to obtain a larger current and transconductance. To investigate the frequency performance of the nvFET, the unit current gain cutoff frequency  $f_t$  is used as a test parameter, and the unit current gain cutoff frequency  $f_t$  can be calculated by the following Equation 2

$$f_t = g_m / 2\pi C_{in} \quad (2)$$

where  $C_{in}$  is the input capacitance of the transistor. To achieve high-frequency applications of nvFETs, the input capacitance needs to be reduced while increasing the transconductance, which requires optimisation of the device geometry.

The preparation process used in this study can reliably prepare devices with a minimum linewidth of about 50 nm and a minimum line spacing of 30 nm. We used the Multiphysics field simulation software, COMSOL Multiphysics 6.2, to simulate the electrical performance of the devices, to reliably prepare high  $f_t$  nvFETs, and to consider the optimisation of the geometrical parameters. The general flow of the simulation to solve the device operating state includes: building a geometrical model of the nvFET and defining the materials of the electrodes, dielectrics, and peripheral vacuum channel in the physical field; delineating the mesh, and refining the mesh on the surface of the source since the source geometry of the nvFET and the strength of the electric field on the micro-region are critical; solving for the electrostatic field to obtain a high-quality electric field distribution as well as capacitance characteristics of the source; and performing the simulation in the charged particle tracking physical field with adaptive time-stepping to simulate the transport process of vacuum electrons in the device; post-processing to obtain the data of interest.

Whether the geometry of the source is favourable for FN emission is crucial for the electrical performance of the nvFET, so it is necessary to simulate the structure of the source first. To exclude the interference of the gate, the nvDiode consisting of the source and drain is studied first. Since electron beam exposure is used to define the source electrode pattern, we designed a flat cathode without transition and a cathode with a rounded transition by considering the proximity effect of the mask plate pattern during fabrication. The I-V characteristics are simulated, and the simulation results are shown below. Where the transition fillet radius is 5nm 15nm and 25nm, for the 25nm fillet transition source, the cathode currently is an ideal half circle; in all models, the channel length is controlled at 30nm, the cathode and anode materials are selected Au, the substrate is the same as the structure of the proposed nvFETs, for 80nm silicon oxide on silicon.

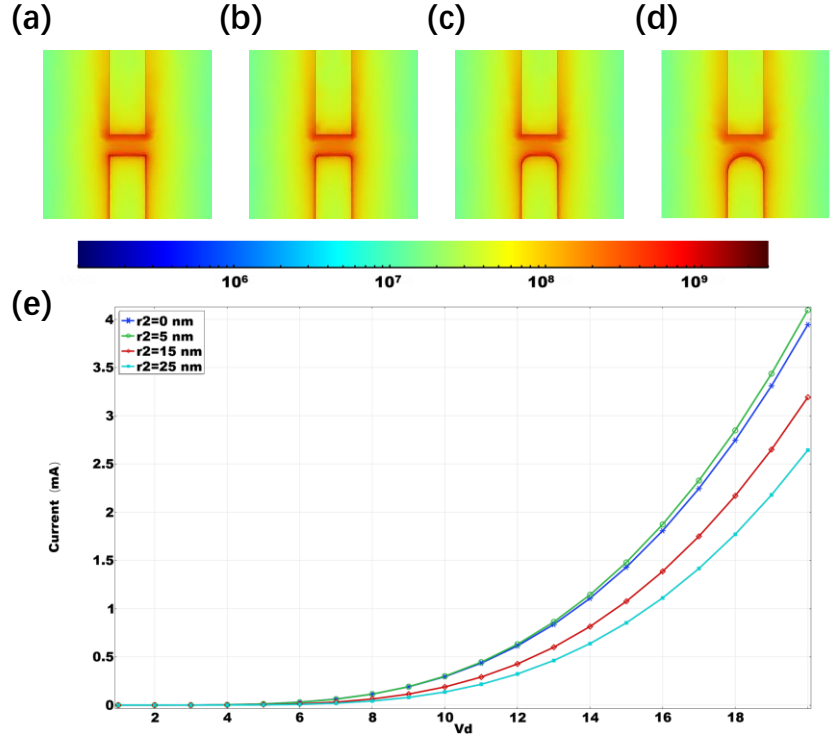


**Figure 4.** (a-d) Electric field distributions (V/m) at the source-drain electrode as nvDiode  $V_s$  ( $V_d$ ) = 20 V: (a) ideal right-angle transition source; (b) non-ideal source with 5 nm rounded approximation; (c) 15 nm rounded approximation; (d) 25 nm radius rounded approximation, which is equivalent to the source in a semicircular approximation; (e) nvDiode with different source structures I-V characteristic curves for different source structures.

For short-channel nvDiode where the source line width is larger than the channel length, the non-ideal source with a smaller transition radius (5 nm) emits the largest cathode current, which is probably because the surface of the source at the transition contributes more to the larger current density compared to the right-angle transition, and the semicircular profile of the source in the shorter channel attenuates the contribution of the current at the edges. By adjusting the appropriate e-beam lithography exposure parameters, a source pattern closer to the non-ideal transition described above can be obtained more consistently.

### 3.2 Capacitor de-embedding simulation and calibration parts

After determining the cathode size of the nvDiode, a gate located in silicon oxide that is embedded is added, and the gate width is set to 50 nm to minimise the input capacitance. The projected position of the gate on the horizontal plane is investigated as an adjustable parameter to optimise the performance of the device.

Adjusting the horizontal position of the gate, since at this time we are concerned with the gate's role in regulating the current, the gate is offset to the drain as a positive displacement, to study the transfer characteristics of the transistor at different gate positions, as shown in Figure 5(a-b), and its input capacitance, as shown in Table 1. When the gate is shifted below the source, the maximum cutoff frequency is obtained at this time according to Equation 2 and the cutoff frequency obtained from the simulation is 2.94 THz. The potential distribution and free electron trajectory tracking during device conduction are shown in Figure 5(c-d).

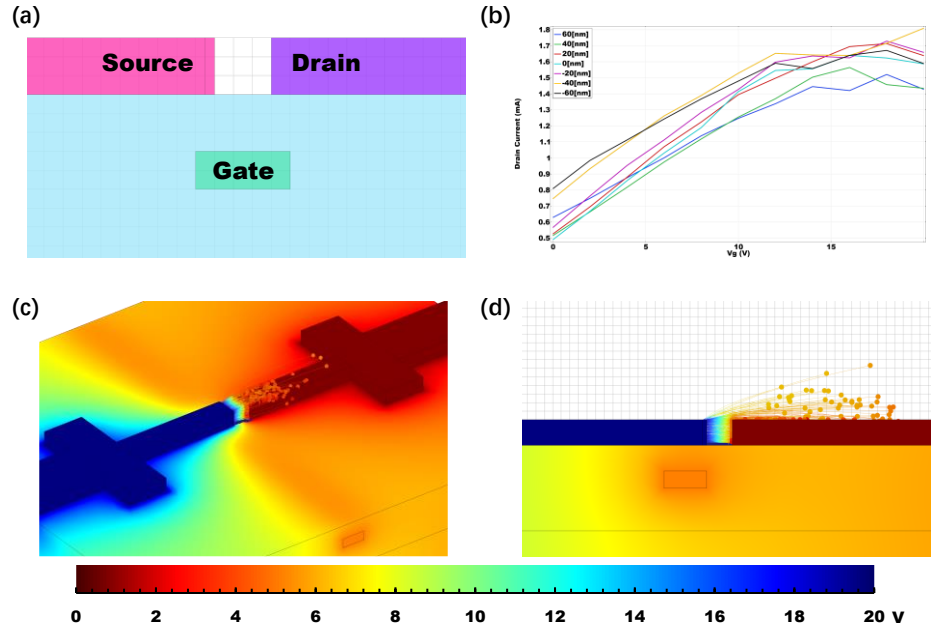


**Figure 5.** (a) Side-view profile of the nvFET; (b) transfer characteristic curve with adjusted gate position; (c) Simulation result of the field emission and electron trajectory of nvFET for  $V_d = 20$  V,  $V_g = 15$  V; (d) Field emission and electron trajectories in profiles of nvFET channels

**Table 1.** Effect of gate horizontal position offset on input capacitance

Gate Shift (nm)	-60	-40	-20	0	20	40	60
$C_{in}$ (aF)	5.873	5.815	5.766	5.742	5.769	5.815	5.832

To achieve a comprehensive on-chip test to obtain the cut-off frequency of the transistor, consideration needs to be given to designing an appropriate capacitance test method. As can be seen in Table 1, the input capacitance of the transistor is about  $10^{-18}$  F, which cannot be directly measured by existing capacitance measurement equipment. Testing multiple nvFETs in parallel so that the total input capacitance is of the same order of magnitude as the parasitic capacitance of the test fixture is a viable option for testing.

Figure 6a examines whether the input capacitance of the nvFET in parallel approximately conforms to a linear law with respect to the number of parallel connections. The linear law of the number of transistors versus capacitance indicates that a more accurate measurement of the input capacitance of a single nvFET can be obtained by de-embedding.

Finally, the parasitic capacitance between the probes used for capacitance testing, Pad to substrate, and each other was tested, with a total parasitic capacitance in the order of  $10^{-15}$  F. For this purpose, at least 1000 nvFETs need to be connected in parallel to obtain reliable capacitance results. Figure 6(b-e) shows the layout design of 1000 nvFETs and corresponding calibration parts with localised SEM imaging of the device.

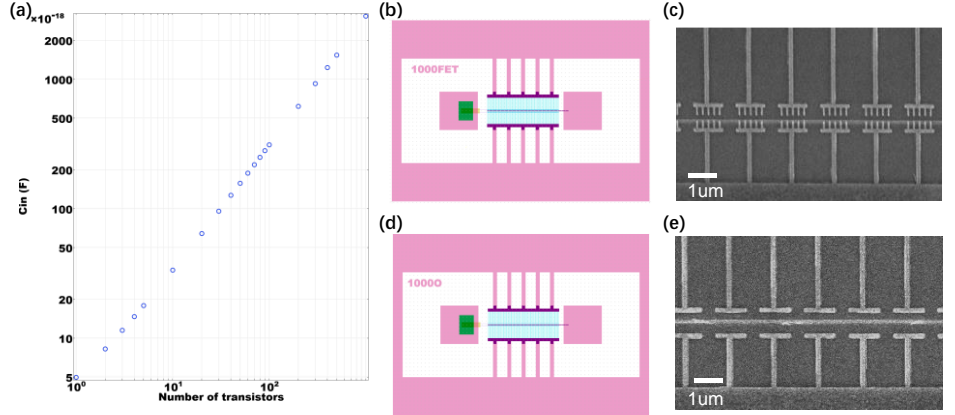


**Figure 6.** (a) Relationship between the increasing number of transistors in parallel and the input capacitance; (b-c) Plates and local SEM images of 1000 nvFETs in parallel; (d-e) SEM images of the calibrated parts used for the corresponding de-embedding and localized

### 3.3. Device Performance Measurement

The prepared nvFET arrays obtained in parallel in groups of 1000 nvFETs, Figure 6(b-c), were used for capacitance tests, and individual nvFETs, Figure 7(a-b), were used for current characterisation tests, all the tests were carried out inside the vacuum probe stage, and the sample stage was heated under vacuum at 120°C and kept for 1h before testing to remove the gases and water vapour adsorbed on the surface of the device, if no. It is also noted that the temperature on the chip was controlled at 25°C and the ambient pressure was  $1.1 \times 10^{-2}$  Torr during the test. The test site diagrams are shown in Figure 7(c-d).

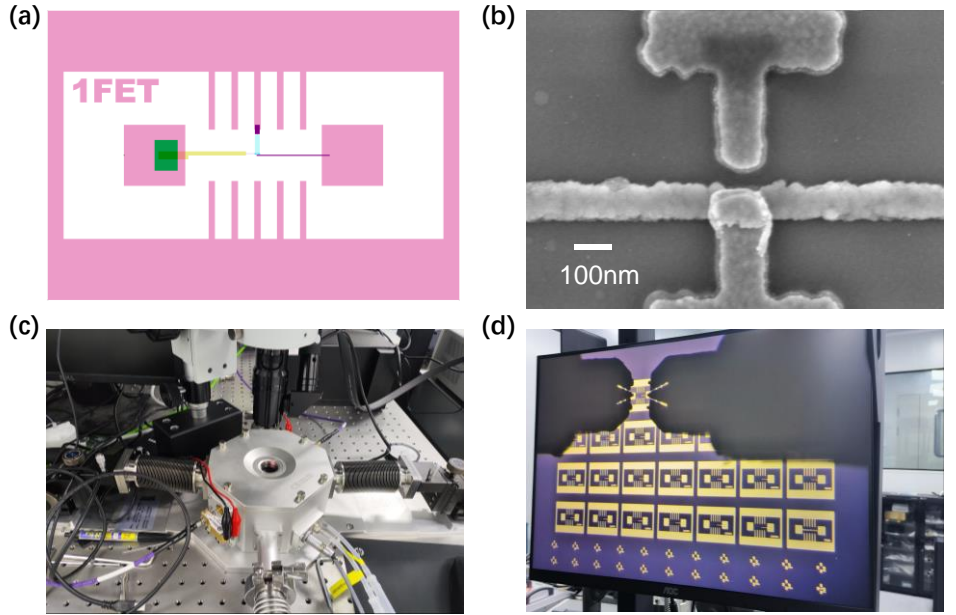


**Figure 7.** (a) Plate of a single nvFET with GSG probe contacts for testing; (b) SEM imaging of a single nvFET; (c-d) test site where electrical tests are performed

The input capacitance of the device was tested using a capacitance meter,  $122.15 \pm 0.42$  fF for 6 sets of capacitance calibrators and  $128.46 \pm 0.40$  fF for 24 sets of 1000 nvFETs. After de-embedding, the average input capacitance of 1000 nvFETs in parallel was 6.31 fF, and the input capacitance of a single nvFET was 6.3 aF.

The I-V characteristics of the individual nvFETs were tested using a source meter, in which the source was placed at 0 V and reciprocal scans were performed to exclude current contributions from parasitic capacitances. The transfer characteristic curve of the device is shown in Figure 8a to test whether the drain current is contributed by the FN

emission current, the transfer characteristic was examined using a distortion of Equation 1, as shown in Figure 8b. Since the gate overlaps the source in the vertical direction, the quality of the gate buried layer was additionally checked, as shown in Figure 8c. The buried gate effectively reduces gate leakage. The measured maximum transconductance is  $66.9 \mu\text{S}$ , and the cutoff frequency of the device is 1.69 THz according to Equation 2.

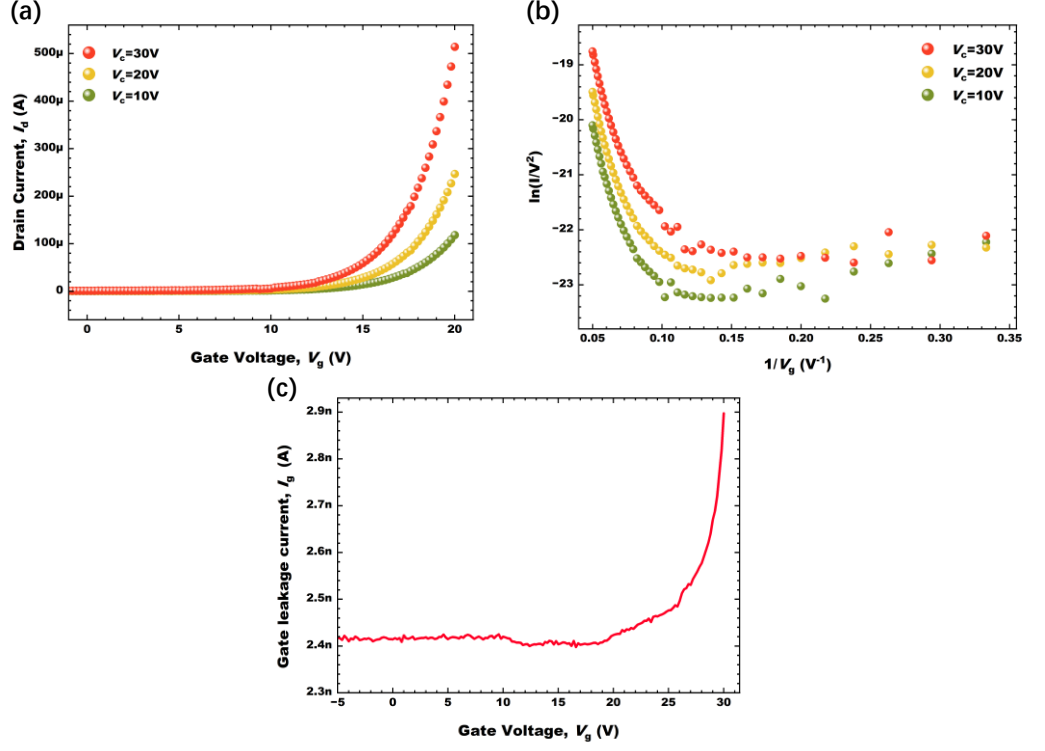


**Figure 8.** Electrical performance of a single nvFET (a) transfer characteristic; (b) F-N emission current fitting curve; (c) gate leakage current

In addition, the devices were tested for temperature and irradiation stability. The temperature of the device was tested by changing the carrier temperature and then holding it for 10mins to ensure that the temperature of the device reached the set level. Four sets of conformance-tested samples were sent to the Shanghai Institute of Applied Physics for  $\gamma$ -ray irradiation at natural radiation (blank control group), 25 krad, 50 krad, and 100 krad. nvFETs showed good stability in both temperature and irradiation tests, as shown in Figure 9.

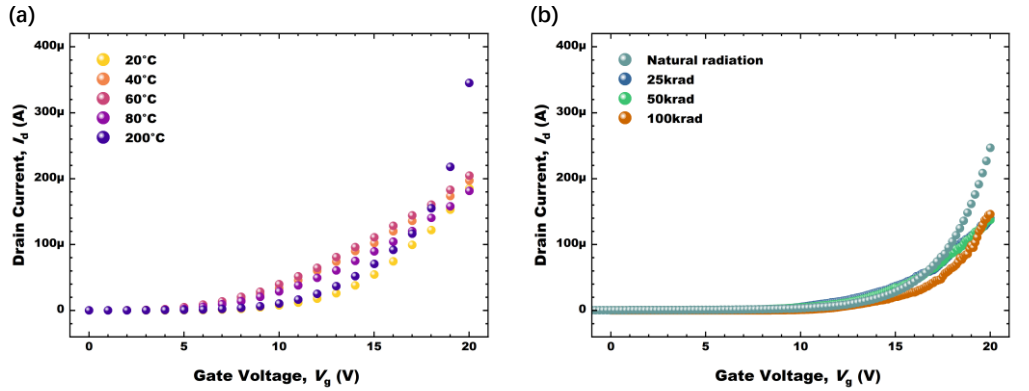


**Figure 9.** Device stability measurements (a) transfer characteristics of individual nvFETs versus temperature; (b) irradiation stability of individual nvFETs

#### 4. Discussion and Conclusions

In this paper, a nvFET with a buried gate structure is proposed, which has a high field emission efficiency and a terahertz-level cutoff frequency based on the results of simulation and preparation tests. The buried gate structure reduces the gate-source leakage current, and the process is fully compatible with the existing MOSFET process. At the same time, the configuration is suitable for parallel connection of multiple devices or integration with conventional semiconductor devices, and it is easy to realise on-chip heterostructure preparation, which can bring into full play the unique advantages of the nvFET in high-power and high-frequency applications.

To further improve the cutoff frequency of the nvFETs, the authors believe that the use of low-K dielectrics as the buried gate dielectric layer[22], as well as the replacement of the Au source with a low figure-of-merit material, are both feasible and valuable studies[3,18]. Our future research directions will include continuing to optimise the structural design to achieve higher electron harvesting efficiency, testing the long-term stability of the device, and extending the proposed device to practical RF applications.

**Author Contributions:** Methodology, W.H. and B.H.; software, Y.H. and G.G.; device manufacture Y.H., Z.K. and J.L.; data curation, Z.K., G.G. and F.G.; writing—original draft preparation, Y.H. and Z.K.; writing—review and editing, W.H.; visualization, Y.H. and M.L.; supervision, W.H.; project administration, W.H. and B.H.; funding acquisition, W.H. All authors have read and agreed to the published version of the manuscript.

**Funding:** This research was funded by the Shenzhen Science and Technology Program, grant number JCYJ20200109105415835 and KQTD20200820113046084.

**Data Availability Statement:** All material described in the manuscript, including all relevant raw data, will be made freely available to any scientist who wishes to use it for non-commercial purposes without violating participant confidentiality.

**Acknowledgments:** We would like to express our gratitude to the Optoelectronics Center of Shenzhen University and SuPro Instruments for their invaluable assistance and technical support during the development of this project.

**Conflicts of Interest:** The authors declare no conflicts of interest.

## References

1. Han, J.-W.; Sub Oh, J.; Meyyappan, M. Vacuum Nanoelectronics: Back to the Future?—Gate Insulated Nanoscale Vacuum Channel Transistor. *Appl. Phys. Lett.* **2012**, *100*, 213505, doi:10.1063/1.4717751.
2. Assis, T.A. de; Dall’Agnol, F.F.; Forbes, R.G. Field Emitter Electrostatics: A Review with Special Emphasis on Modern High-Precision Finite-Element Modelling. *J. Phys.: Condens. Matter* **2022**, *34*, 493001, doi:10.1088/1361-648X/ac920a.
3. Han, J.-W.; Seol, M.-L.; Moon, D.-I.; Hunter, G.; Meyyappan, M. Nanoscale Vacuum Channel Transistors Fabricated on Silicon Carbide Wafers. *Nat Electron* **2019**, *2*, 405–411, doi:10.1038/s41928-019-0289-z.
4. Deka, N.; Subramanian, V. On-Chip Fully Integrated Field Emission Arrays for High-Voltage MEMS Applications. *IEEE Transactions on Electron Devices* **2020**, *67*, 3753–3760, doi:10.1109/TED.2020.3006167.
5. Khoshbujari, F.K.; Sharifi, M.J. Finger Gate Vacuum Channel Field Emission Transistors: Performance and Sensitivity Analysis. *IEEE Transactions on Electron Devices* **2021**, *68*, 5250–5256, doi:10.1109/TED.2021.3100013.
6. Johnson, E.O. Physical Limitations on Frequency and Power Parameters of Transistors. In *Semiconductor Devices: Pioneering Papers*; WORLD SCIENTIFIC, 1991; pp. 295–302 ISBN 978-981-02-0209-5.
7. Tao, H.; Wang, Q. Study on Ballistic Transport Electronics—A Vacuum Field Emission Transistor with Carbon Nanotube Cold Cathode. In Proceedings of the 2023 24th International Vacuum Electronics Conference (IVEC); April 2023; pp. 1–2.
8. Zhao, S.; Ding, H.; Li, X.; Cao, H.; Zhu, Y. The Selection and Design of Electrode Materials for Field Emission Devices. *Materials Science in Semiconductor Processing* **2023**, *167*, 107804, doi:10.1016/j.mssp.2023.107804.
9. Heo, S.J.; Shin, J.H.; Jun, B.O.; Jang, J.E. Vacuum Tunneling Transistor with Nano Vacuum Chamber for Harsh Environments. *ACS Nano* **2023**, *17*, 19696–19708, doi:10.1021/acsnano.3c02916.
10. Veen, G.N.A. van Space-charge Effects in Spindt-type Field Emission Cathodes. *Journal of Vacuum Science & Technology B: Microelectronics and Nanometer Structures Processing, Measurement, and Phenomena* **1998**, *12*, 655, doi:10.1116/1.587407.
11. Talin, A.A.; Dean, K.A.; Jaskie, J.E. Field Emission Displays: A Critical Review. *Solid-State Electronics* **2001**, *45*, 963–976, doi:10.1016/S0038-1101(00)00279-3.
12. Spindt, C.A. A Thin-Film Field-Emission Cathode. *Journal of Applied Physics* **2003**, *39*, 3504, doi:10.1063/1.1656810.
13. Xu, J.; Lin, C.; Shi, Y.; Li, Y.; Zhao, X.; Zhang, X.; Zhang, J. Optimization of a Field Emission Electron Source Based on Nano-Vacuum Channel Structures. *Micromachines* **2022**, *13*, 1274, doi:10.3390/mi13081274.
14. J. -W. Han; J. S. Oh; M. Meyyappan Cofabrication of Vacuum Field Emission Transistor (VFET) and MOSFET. *IEEE Transactions on Nanotechnology* **2014**, *13*, 464–468, doi:10.1109/TNANO.2014.2310774.
15. Han, J.-W.; Moon, D.-I.; Meyyappan, M. Nanoscale Vacuum Channel Transistor. *Nano Lett.* **2017**, *17*, 2146–2151, doi:10.1021/acs.nanolett.6b04363.
16. Fan, L.; Bi, J.; Xi, K.; Zhao, B.; Yang, X.; Xu, Y. Sub-10-Nm Air Channel Field Emission Device With Ultra-Low Operating Voltage. *IEEE Electron Device Letters* **2021**, *42*, 1390–1393, doi:10.1109/LED.2021.3095475.
17. Chen, T.; Hong, W.; Shen, C.; Fan, H.; Bai, N.; Sun, X. High Gain Double Gate Vacuum Emission Transistor with Low Leakage Current. In Proceedings of the 2021 22nd International Vacuum Electronics Conference (IVEC); April 2021; pp. 1–2.
18. Xu, J.; Lin, C.; Li, Y.; Zhao, X.; Shi, Y.; Zhang, X. Structure Optimization of Planar Nanoscale Vacuum Channel Transistor. *Micromachines* **2023**, *14*, 488, doi:10.3390/mi14020488.
19. Lang, S.A. Unification of Electron Emission Mechanisms: From Liquids to Lasers. **2020**, doi:10.25394/PGS.13366652.v1.
20. Fowler, R.H.; Nordheim, L. Electron Emission in Intense Electric Fields. *Proceedings of the Royal Society of London. Series A, Containing Papers of a Mathematical and Physical Character* **1928**, *119*, 173–181, doi:10.1098/rspa.1928.0091.
21. Ellis, R.K. Fowler-Nordheim Emission from Non-Planar Surfaces. *IEEE Electron Device Letters* **1982**, *3*, 330–332, doi:10.1109/EDL.1982.25590.
22. Zhou, P.; Chen, J.; Tang, S.; Yu, J.; Wang, C.; Li, H.; Lu, H.; Yan, P.; Hou, D.; Chen, Z.; et al. Research on Silicon-Based Terahertz Communication Integrated Circuits. *Chinese Journal of Electronics* **2022**, *31*, 516–533, doi:10.1049/cje.2021.00.253.